



Architected hybrid conductors: Aluminium with embedded copper helix

R. Lapovok^{a,b,*}, V.V. Popov Jr^c, Y. Qi^a, A. Kosinova^a, A. Berner^a, C. Xu^{a,d}, E. Rabkin^a, R. Kulagin^e, J. Ivanisenko^e, B. Baretzky^e, O.V. Prokof'eva^f, A.N. Sapronov^f, D.V. Prilepo^f, Y. Beygelzimer^g

^a Department of Materials Science and Engineering, Technion – Israel Institute of Technology, Haifa 3200003, Israel

^b Institute for Frontier Materials, Deakin University, Waurn Ponds, Vic 3216, Australia

^c Israel Institute of Metals, Technion Research & Development Foundation Ltd., Israel

^d School of Materials Science and Engineering, Xi'an University of Technology, Shaanxi 710048, China

^e Institute of Nanotechnology, Karlsruhe Institute of Technology, Eggenstein-Leopoldshafen 76344, Germany

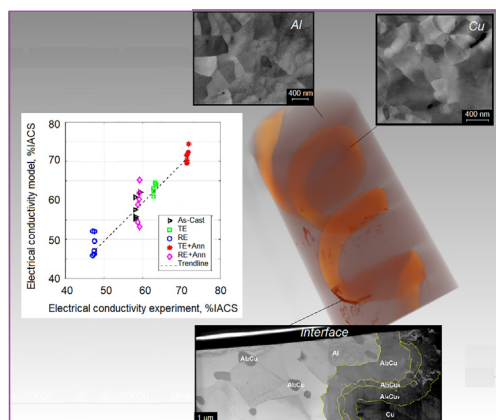
^f Donetsk Institute for Physics and Engineering named after A.A. Galkin, 83114 Donetsk, Ukraine

^g Donetsk Institute for Physics and Engineering named after A.A. Galkin, National Academy of Sciences of Ukraine, 03028 Kyiv, Ukraine

HIGHLIGHTS

- The new design for Al–Cu conductor with copper used as helical wire fully embedded in the aluminium matrix is suggested.
- Samples with helical reinforcement exhibit increased load-bearing capability and higher strain hardening during deformation.
- The SPD processing is important for strengthening of the hybrid due to grain refinement and dissolution of intermetallic.
- New analytical model predicting the electrical conductivity of hybrids and accounting for intermetallic layer is developed.
- The model depends on two parameters determined by copper volume fraction and the geometry of the helical constituent.

GRAPHICAL ABSTRACT



ARTICLE INFO

Article history:

Received 27 August 2019

Received in revised form 1 December 2019

Accepted 2 December 2019

Available online 06 December 2019

Keywords:

Copper-aluminium hybrid materials

Conductivity

Interface

Intermetallic

ABSTRACT

This study is inspired by the potential of application-designed aluminium-copper conductors. This work combines recently discovered advantages of hybrids with one constituent having a helical architecture with the benefits provided by severe plastic deformation (SPD) methods. The hybrids are made by embedding copper helices in melted aluminium and subjecting cast hybrid ingots to different SPD techniques. The electrical conductivity, microstructure features and strength of the produced samples are discussed in relation to effect of SPD and annealing on both constituents and an interface zone formed during the hybrids' production. It was shown that between all processing techniques the reciprocal extrusion (RE) has the great potential for production of lightweight conductors with high conductivity and enhanced strength. A new model describing the effective electrical conductivity of hybrid samples, consisting of an aluminium matrix with an embedded copper helix and intermetallic containing interface, is developed and justified by experimental data. The model is shown to

* Corresponding author at: Department of Materials Science and Engineering, Technion – Israel Institute of Technology, Haifa 3200003, Israel.

E-mail address: r.lapovok@deakin.edu.au (R. Lapovok).

be instrumental for analysis of the effect of the helix's parameters and interface width on effective conductivity of the hybrid samples and could be used for optimal design of hybrid conductors.

© 2019 The Authors. Published by Elsevier Ltd. This is an open access article under the CC BY-NC-ND license (<http://creativecommons.org/licenses/by-nc-nd/4.0/>).

1. Introduction

Copper and aluminium are the two metallic materials with the lowest electrical resistivity used to make electrical conductors. While pure copper has the best conductivity, which is taken as 100% IACS (International Annealed Copper Standard), aluminium offers lower cost and a lighter weight. The choice between copper and aluminium is defined by their area of applications. Copper and copper alloys, without doubt, are the first choice for electronic and telecom wires [1], while aluminium and aluminium alloys are the best selection for overhead high-voltage power lines [2]. Due to aluminium's lower conductivity (65% vs. 100%), however, the aluminium conductor must be larger than an equivalent copper one to achieve the same efficiency. Additionally, copper is twice as strong as aluminium, which means that an aluminium wire cross-section must be double that of the copper one to get the same load-bearing capacity as copper wire.

To benefit from the best properties of both materials, an application-designed hybrid composed of aluminium and copper seems a reasonable solution. Industry seems to be moving toward such a solution. Recently, for example, a combined Al/Cu cable was used at the Dietlikon Power Station in Switzerland as a low-voltage underground cable possessing the technological properties of copper at the price of aluminium [3]. Low-cost requirements have, unfortunately, limited the volume fraction of copper in aluminium conductors and, therefore, the tensile strength increase by a copper addition to aluminium conductors has, thus far, not been significant.

In the last two decades, a significant effort has been invested in developing severe plastic deformation (SPD) techniques, which impart a virtually unlimited amount of shear strain into materials [4]. The shearing and accompanying material rotations result in extreme grain refinement, down to the nanometer-range. It was demonstrated that by forming an ultrafine-grained (UFG) structure, a much more significant increase in the strength of conductive aluminium and copper alloys can be achieved [5]. Nevertheless, simultaneously with grain size decrease, there is corresponding increase in the grain boundary and dislocation densities, which consequently leads to reduction of electrical conductivity due to the well-known relation between strength and electrical conductivity [6]. Designing a process in which SPD of different alloys is followed by heat treatment to recover the defects introduced by SPD but that maintains the UFG structure may be a reasonable strategy for achieving a high level of both properties—strength and conductivity [5]—in the resulting composite material.

Today, accordingly, the focus shifts on determining the optimal design of the constituents of hybrid materials to benefit from their advantages. In a visionary article about new ways to design novel materials, Ashby [7] highlighted the potential of hybrid materials, which he defined as combinations of two or more materials assembled in such a way as to have attributes not offered by either one alone. The material design strategies championed by Ashby are inspired by geometry and introduce shapes and arrangements of the building blocks to enable new 'degrees of freedom' for hybrids [8,9]. This geometric aspect defines hybrid materials as a special case of composites with engineered inner architectures.

The present research focuses on the spiral geometry of copper helices in aluminium bars, which can contribute to enhancement of hybrid conductor properties. Helical architectures are very common in natural biological systems, ensuring a combination of high strength and stretchability [10]. In engineered structures, the beneficial effect of

reinforcement of a material with helical inclusions on the Young's modulus, strain hardening and tensile ductility was demonstrated in [11].

Here we study the helical architecture of the copper constituent in a Al/Cu composite in conjunction with different SPD processing techniques and low temperature annealing for optimisation of the hybrid material's strength and electrical conductivity.

Special attention is paid to the evolution of intermetallic phases formed at the aluminium – copper interface during processing. Such intermetallics are known to exhibit lower conductivity than the respective pure components, which, in addition to their intrinsic brittleness, can compromise the beneficial effects of material hybridization. The possibility of intermetallic zone tailoring by SPD is discovered.

2. Materials and methods

2.1. Samples preparation

Samples were prepared by pouring melted pure aluminium (99.96%) into crucibles where the helix, made from commercially pure copper (99.99%), was placed along the central axis of the vessel. The set of copper helices were made from copper wire with diameters, d , 1.5 and 5 mm and with different pitch, p , external diameters, D , and internal diameters, as shown in Table 1.

To evaluate the temperature increase in the copper wire during casting, the convective heat transfer from hot aluminium to copper can be calculated as, [12]:

$$\frac{dq}{dt} = hS[T_{Al} - T(t)], \quad (1)$$

and the heat flux can be estimated from the following expression:

$$dq = mk_{Cu}dT(t), \quad (2)$$

where $h = 1000 \text{ (Wm}^{-2}\text{K}^{-1}\text{)}$ [13] is the heat transfer coefficient at the copper-aluminium interface; $S = \pi DL$ is the surface area of copper wire; $T_{Al} = 660 \text{ }^\circ\text{C}$ is the aluminium's initial temperature; $T(t)$ is the temperature of the copper wire with mass m , which rises from an initial temperature of $T(0) = 20 \text{ }^\circ\text{C}$ to an equilibrium temperature of $0.99T_{Al} = 653 \text{ }^\circ\text{C}$, and $k_{Cu} = 0.385 \text{ (J }^\circ\text{C}^{-1}\text{g}^{-1}\text{)}$ [12] is the heat capacity coefficient per unit mass.

Integrating Eqs. (1) and (2) gives an estimation of the time needed until temperature equilibrium is reached:

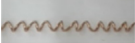




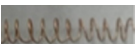

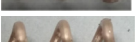

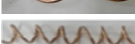
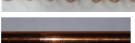
$$t = \frac{mk_{Cu}}{hS} \ln \frac{T_{Al} - T(0)}{T_{Al} - T(t)} = \frac{mk_{Cu}}{hS} \ln \frac{T_{Al} - 20}{T_{Al} - 0.99T_{Al}}. \quad (3)$$

Using Eq. (3) for all samples showed that equilibrium temperature was reached at a time within the range of (6...14) seconds.

The cast billets were then machined into samples with geometry required for the three different SPD processes used in this research and described below.

Samples 1 and 2 containing helices with an internal diameter of 4 mm were cut into three rods, each with a 12-mm diameter and 35-mm long, and deformed at room temperature by high pressure torsion extrusion (HPTE); a detailed description of the process is given in [14]. This process combines the benefits of two deformation techniques, namely, extrusion and high pressure torsion. The samples were extruded with a translation speed of 10 mm/min through sectional

Table 1
Parameters of the copper helices and deformation processes used.

Helix image	Rod number	Wire diameter d, mm	Helix internal diameter D-d, mm	Helix pitch p, mm	Deformation process
	1	1.5	4	6	HPTE
	2	5	4	24	HPTE
	3	1.5	15	12	RE
	4	5	15	25	RE
	5	5	15	30	RE
	6	1.5	15	15	TE
	7	5	10	24	TE
	8	5	10	18	TE
	9	5	4	31	TE
	10	1.5	10	10	TE
	11	5	0	∞	Non-deformed

containers rotating relative to each other, with an angular speed of 5 rev/min and an average accumulated equivalent strain of about 930%.

Samples 3, 4 and 5 containing helices with an internal diameter of 20 mm were deformed at 400 °C by four passes through a reciprocal extrusion (RE) process [15]. Here, samples were extruded back and forth between two chambers of equal size (35 mm in diameter) connected via a narrow opening (10 mm in diameter) with a die set in the shape of an hourglass. Each pass introduced an equivalent strain about 250% into the deformed material. Consequently, the total accumulated average equivalent strain was about 1000%.

Samples 6, 7, 8, 9 and 10 containing helices with different diameters were machined into parallelepipeds (40 × 25 × 80 mm) and deformed by two passes through a twist extrusion (TE) [16] process, at 200 °C and back-pressure of 50 MPa with a total average accumulated equivalent strain ranging between 30% and 120%.

After the deformation, some samples were subjected to recovery heat treatment at 250 °C for 4 h to retain the ultrafine grain size in the copper constituent and attain recrystallization of the aluminium matrix.

The helix geometry in the deformed samples was imaged by HR 3D μ Computed Tomography using RX Solution's micro-tomograph with an operational voltage of 150 kV and a large area flat panel (~100 × 100 mm²). The reconstruction (from 2D projections to 2D cross-sections) was made with RX Solution's X-Act software, followed by 3D visualisation using Dragonfly software.

2.2. Electrical resistivity measurements

The electrical resistivity for all these samples was measured at room temperature by the four-point method. The resistivity was calculated

Table 2
Characteristics of copper helices essential for conductivity calculation.

Rod number	Winding radius R, mm	Pitch parameter h, mm	Tangent inclination to z axis $\tan\theta$ (θ°)	Copper volume fraction f_{Cu}		
1	2.75	0.95	0.347 (19.15°)	0.024	0.048	0.051
	4.50	3.82	0.849 (40.33°)	0.126	0.138	0.152
3	8.25	1.91	0.231 (13.03°)	0.0034	0.0006	
4	10.00	3.98	0.398 (21.70°)	0.0428	0.0460	
5	10.00	4.77	0.477 (28.36°)	0.0684	0.0131	
6	8.25	2.39	0.288 (16.07°)	0.0015		
7	7.5	3.82	0.509 (26.99°)	0.0536		
8	7.5	2.86	0.382 (20.91°)	0.0594		
9	4.50	4.93	1.096 (52.91°)	0.0311		
10	5.75	1.59	0.277 (15.47°)	0.0034		
11	2.5	∞	0 (0.00°)	Varied		

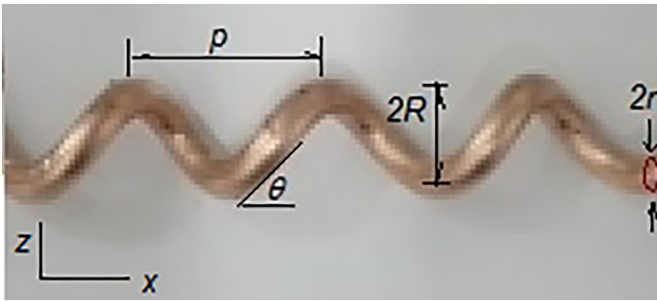


Fig. 1. Helix parameters.

using the following expression:

$$\rho = \frac{V \cdot S}{I \cdot L}, \quad (4)$$

where V is the voltage drop between two probe points (at a distance L from each other) on the side of the parallelepiped measured by a Keithley 2700 multimeter; L is varied from 5 to 55 mm (it was equal to 5 mm, 25 mm, 35 mm and 55 mm as four different probes were used), depending on the specimen's height; and $I = 10 \text{ A}$ is a constant current applied by the TDK-Lambda's power source through the top and bottom sides of the sample.

The base area of the sample, equal to S , is in the contact with copper plates under 200 Pa of pressure.

2.3. Microstructure characterization

SEM characterization was carried out using a Zeiss Ultra Plus high-resolution scanning electron microscope (HR-SEM) at 10 kV accelerating voltage. The majority of images have been taken using the detector of back-scattered (BS) electrons in Z-contrast mode to distinguish different phases. To reveal the grains with different crystallographic orientation at the mirror-polished surface (without etching), the angular

selected BS electrons detector was used at 15 kV accelerating voltage. Chemical analysis was performed by energy-dispersive X-ray spectroscopy (EDX) by HR-SEM at 10 kV accelerating voltage. Cu $L\alpha$ and Al $K\alpha$ analytical lines and pure aluminium and copper standards were used. The average grain size was measured using SEM BS images by line intercept method according to the ASTM (E112 - 10) standard.

Transmission electron microscopy (TEM) was performed using a Techna T20 operated at 200 KeV. Scanning transmission electron microscopy (STEM) was performed with a double Cs-corrected FEI 80-300 Themis G² operated at 300 kV. A 21 mrad beam convergence semi-angle was used. In high-angle annular dark-field (HAADF-) STEM imaging mode, the camera length was set to 94 mm, and gave an inner collection semi-angle of 119 mrad and an outer collection semi-angle of 200 mrad. The bright-field (BF) and dark-field (DF) STEM images were also collected employing the semi-angle range of 0–11 mrad and 15–25 mrad, respectively. Energy-dispersive X-ray spectroscopy (EDX) mapping was carried on STEM using a Dual-X detector (Bruker).

TEM lamella was prepared by the focused ion beam (FIB) technique using a FIB-SEM dual beam microscope (FEI Helios Nanolab Dualbeam G³).

2.4. Helix geometry characterization

Before SPD, the architecture and microstructure of the samples were characterised analytically and experimentally, Table 2.

The helix surface of the copper wire in x, z coordinates, Fig. 1, can be expressed as:

$$(x - R \cdot \cos(z/h))^2 + (y - R \cdot \sin(z/h))^2 = r^2, \quad (5)$$

where R is the winding radius ($D = 2R$), r is the wire radius ($d = 2r$), and h is the parameter defining the pitch of the helix ($p = 2\pi h$).

In parametric form, $t \in (0, 2\pi)$, the helix is expressed as:

$$x(t) = R \cdot \cos(t) \quad y(t) = R \cdot \sin(t) \quad z(t) = h \cdot t, \quad (6)$$

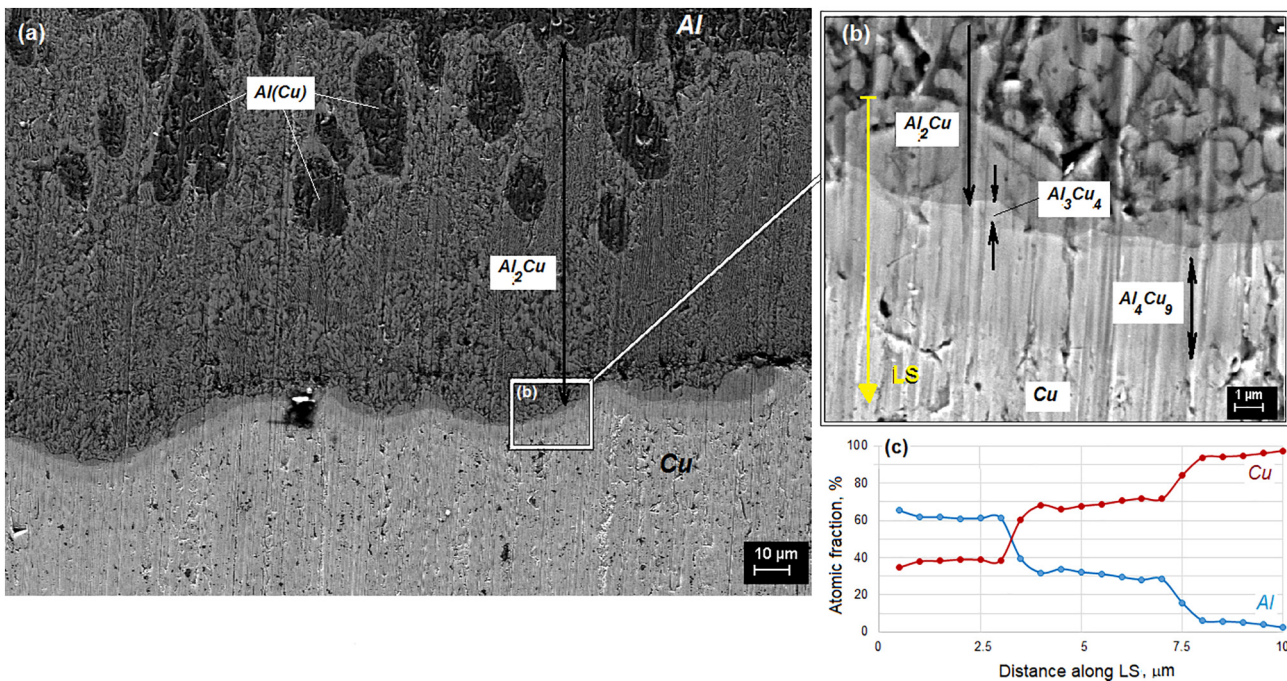


Fig. 2. SEM (BS) images showing the interface zone formed between Al and Cu (EDX has taken along LS shown in insert (b)). (a) The wide ($100 \pm 20 \mu\text{m}$) layer of the θ - Al_2Cu phase with bubble-like inclusion of Cu solid solutes in Al (97at%Al-3at%Cu); (b) The thin ($4 \pm 2 \mu\text{m}$) layer of the γ - Al_4Cu_9 phase and the thinner ($0.7 \pm 0.4 \mu\text{m}$) layer of the ζ - Al_3Cu_4 phase; the yellow line shows the direction of the EDX line scan; (c) The atomic concentration of Al and Cu along the line shown versus distance.

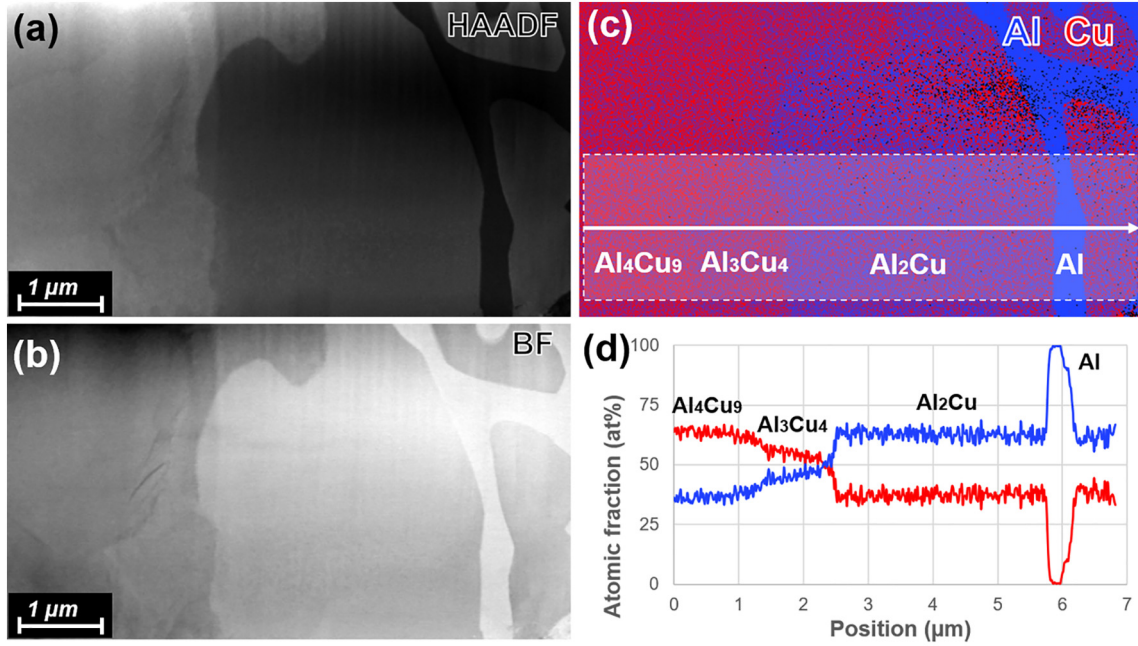


Fig. 3. STEM-EDX analysis showing the chemical composition and grain structure at the interface zone. (a) HAADF-STEM image, (b) BF-STEM image, (c) EDX mapping, (d) chemical composition along the line shown in (c).

and has a constant slope to the z axis defined by angle θ at any point of the surface:

$$\tan\theta = \frac{h}{R} = \frac{p}{2\pi R} \quad (7)$$

Using the data in Table 1, the tangent inclination was calculated for all helices used in this research (see Table 2).

2.5. Copper volume fraction calculations

Despite being able to calculate the helix volume analytically, experimental measurements of the copper volume fraction were made to eliminate the scattering of results due to position of the cut. Each rod was cut into a number of smaller samples according to the requirements of the deformation process along the length of the workpiece. For example, three samples from rods 1 and 2, Table 1, were cut for HPTE processing before deformation, which yielded an average copper volume fraction of 0.041 and 0.139, respectively (see the values in the last column of Table 2). Samples processed by RE (rods 3, 4 and 5, Table 1) were cut into two parts after deformation, yielding large cylindrical samples, 35 mm in diameter, and small cylindrical samples, 10 mm in diameter (see the values in the last column of Table 2). Samples processed by TE (rods 6, 7, 8, 9, 10, Table 1) were not cut into smaller samples.

Diameter of sample 11 was turned down between conductivity measurements to provide the variety of f_{Cu} values necessary to obtain a conductivity baseline.

The required variables were calculated using the weights and dimensions of each sample and the following three equations:

$$W = \hat{\rho}_{Al}V_{Al} + \hat{\rho}_{Cu}V_{Cu} = \hat{\rho}_{Al}(V - V_{Cu}) + \hat{\rho}_{Cu}V_{Cu}, \quad (8)$$

$$V = V_{Al} + V_{Cu}, \quad (9)$$

$$f_{Cu} = \frac{V_{Cu}}{V}, \quad (10)$$

where $\hat{\rho}_{Al}$ and $\hat{\rho}_{Cu}$ are the density of aluminium and copper; V , V_{Al} , V_{Cu}

are the total volume of the sample, the aluminium volume and the copper volume, respectively; and W is the measured weight of the sample.

3. Experimental results and discussion

3.1. Characterization of cast samples

Fig. 2 shows SEM-BS (back-scattered) images of the cross-section of typical samples produced by the technique described in Section 2.1. The solidified aluminium had a typical cast structure while the annealed copper rod had equiaxed grains of $\sim 20 \mu\text{m}$, as defined by line interception method from SEM imaging. The interface between melted aluminium and solid copper came to temperature equilibrium and three layers are visible between the Al and Cu regions. It should be noted, that the cast-aluminium matrix and the interface consisted of intermetallic phases are quite brittle.

The classic Al—Cu phase diagram, analysed by Murray [17], allows thirteen stable intermetallic phases and three metastable phases, in this system. At equilibrium temperature, on an interface equal to $653 \text{ }^\circ\text{C}$: $D_{Cu}^{Al} = 10^{-12} (\text{m}^2 / \text{s})$ and $D_{Al}^{Cu} = 3.98 \cdot 10^{-16} (\text{m}^2 / \text{s})$, where D_{Cu}^{Al} and D_{Al}^{Cu} are the diffusion coefficients of Cu in Al and Al in Cu, respectively. The characteristic diffusion length \sqrt{Dt} was estimated, for 2 h cooling time, to be $85 \mu\text{m}$ for Cu in Al and $1.7 \mu\text{m}$ for Al in Cu. This approximation, however, does not account for the change in the diffusion coefficient during phase formation and, therefore, the diffusion distance of Cu in Al was assessed from SEM images to be $100 \dots 150 \mu\text{m}$, while the Al in Cu diffusion distance was below $1 \mu\text{m}$. Among all intermetallic

Table 3
Electrical resistivity and hardness of three Al—Cu phases from the literature.

Phases	θ -Al ₂ Cu	γ -Al ₄ Cu ₉	ζ -Al ₃ Cu ₄	References
ρ , [ohm - m]	11.1	16.5	-	[19]
ρ , [ohm - m]	7.6	17.3–25.9	-	[20]
ρ , [ohm - m]	6.49	18.8	-	[21]
ρ , [ohm - m]	8.7	13.5	12.2	[22]
$HV_{0.001}$, [MPa]	632	636	-	[21]
HV , [kg/mm ²]	720	1160	-	[19]
$H_{0.002}$, [kg/mm ²]	735	-	852	[23]

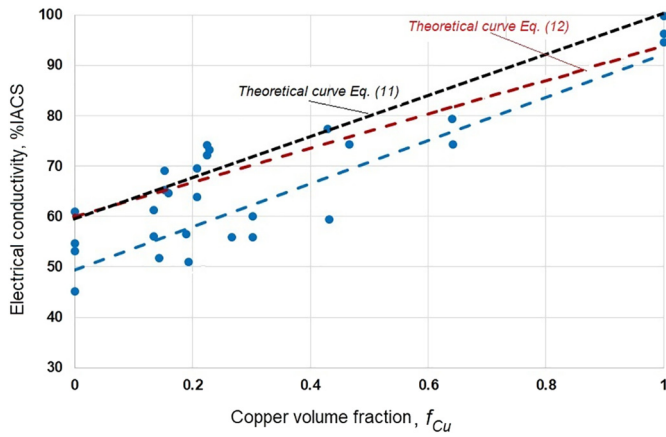


Fig. 4. Electrical conductivity of the cast aluminium billet with a copper straight wire-insert along the axis of the billet versus the copper volume fraction (blue dots are the experimental results; blue dashed line is a linear fitting line). (For interpretation of the references to colour in this figure legend, the reader is referred to the web version of this article.)

compounds (IMC), which have been frequently described in the literature, [18]— θ - Al_2Cu , η - AlCu , ε - Al_2Cu_3 , ζ - Al_3Cu_4 and γ - Al_4Cu_9 —only θ , ζ and γ were found, while high temperature phases were not detected in the cast billets produced for this research.

The chemical composition of the IMC phases was confirmed by STEM-EDX characterization, Fig. 3. The HAADF image and corresponding EDX measurements clearly indicate four phases: Al, θ - Al_2Cu , ζ - Al_3Cu_4 and γ - Al_4Cu_9 . Moreover, in the BF-STEM image, Fig. 3b, grains within each individual four phase were not revealed, which means that these phases were not polycrystalline. Therefore, it could be assumed that the grain size of the IMC is in the micrometre range.

Several studies on aluminium-copper IMCs have shown that all of them are hard and brittle and their electrical resistivity is much higher than of the constituents of this hybrid material, [19–23]. The properties of three phases published previously are summarised in Table 3.

Table 4
SEM (BS) images of copper and aluminium constituents and their interface zone.

	RE ($T = 400\text{ }^\circ\text{C}$, $\varepsilon = 10$)	TE ($T = 200\text{ }^\circ\text{C}$, $\varepsilon = 0.75$)	HPTE ($T = 20\text{ }^\circ\text{C}$, $\varepsilon = 9.3$)
Cu			
Al			
Interface zone			

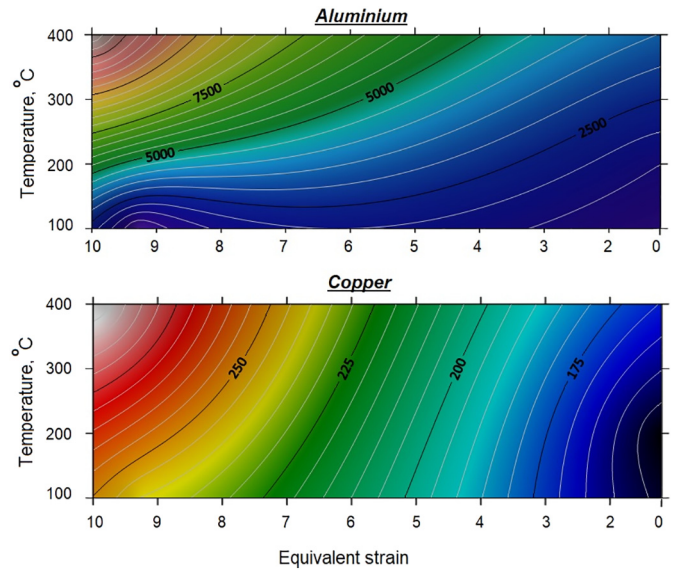


Fig. 5. Grain size of the copper and aluminium constituents of the hybrid samples after deformation.

For comparison, electrical resistivity of pure aluminium is $2.655 - 2.826\text{ } \text{ohm} - \text{m}$ and electrical resistivity of pure copper is $1.707 - 1.724\text{ } \text{ohm} - \text{m}$ [24], while hardness of pure aluminium is around 20 HV and hardness of pure copper is about 57 HV.

3.2. Electrical conductivity as a function of the copper volume fraction for a non-helix shaped constituent

Using sample 11, we eliminated the helix shape parameters from our electrical resistivity study. Sample 11 consisted of a straight wire 5 mm in diameter, cast into an aluminium billet. The electrical conductivity of the cast aluminium was checked on the separately cast aluminium billet and was $53.5 \pm 5.6\%$ IACS. The electrical conductivity of

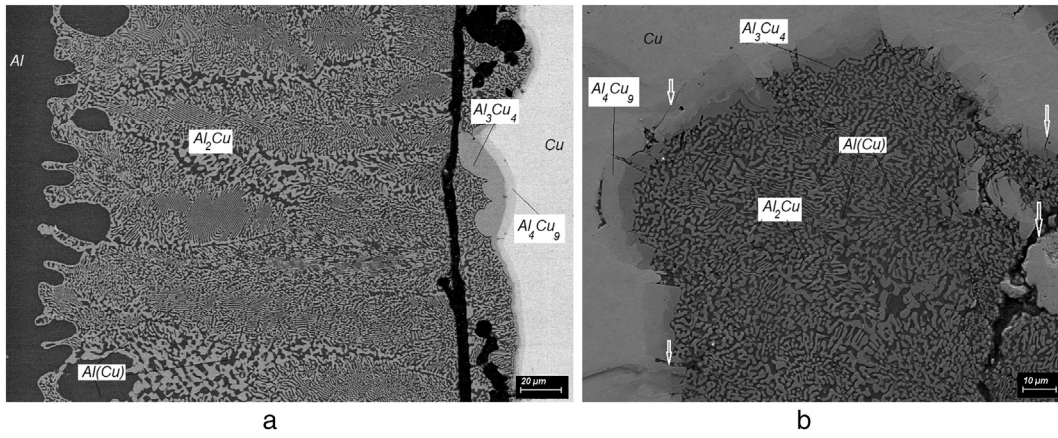
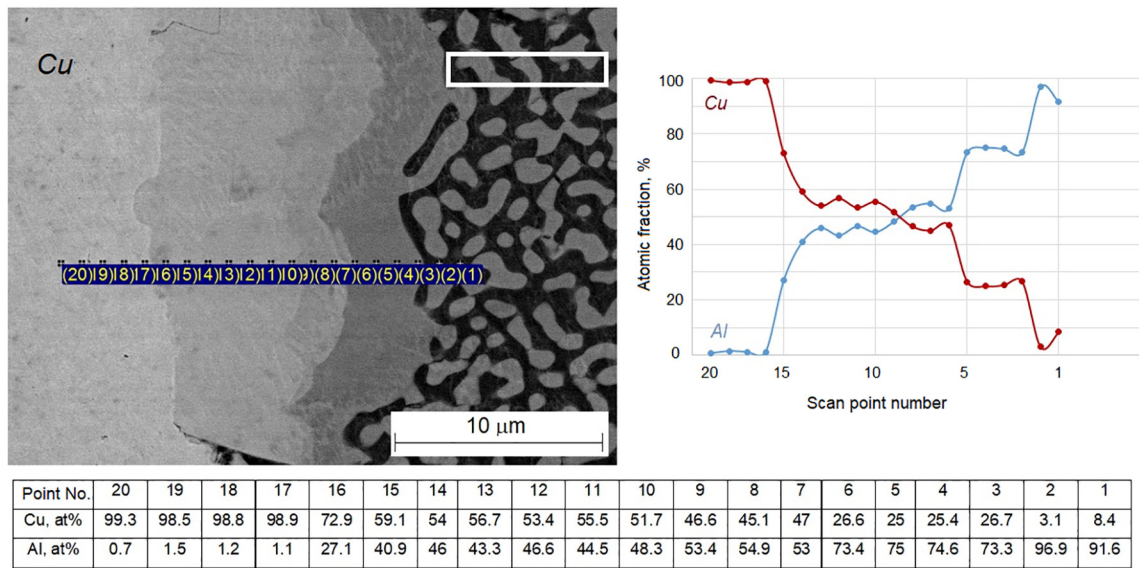
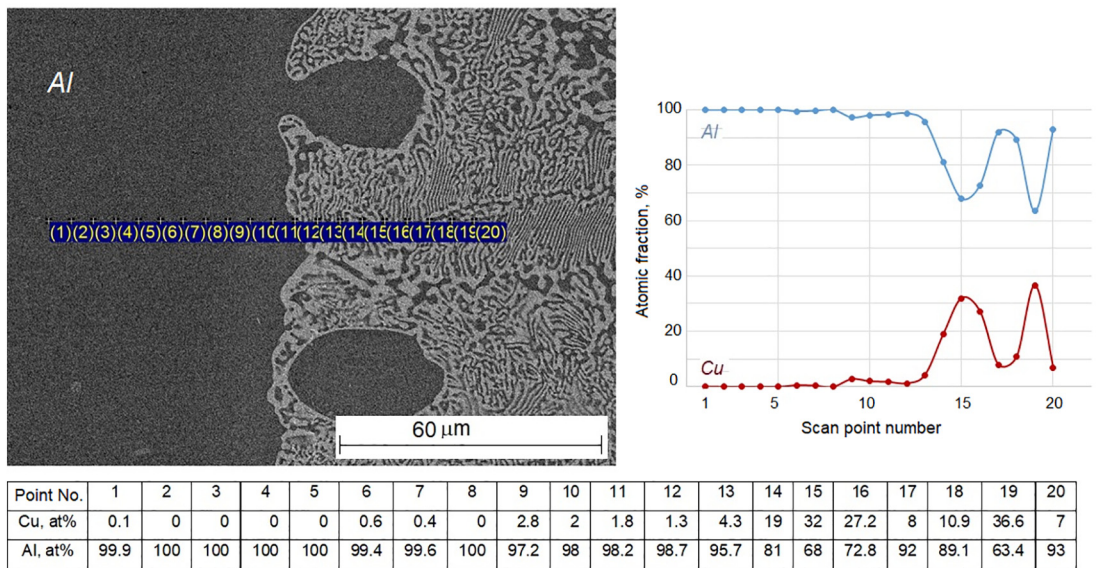


Fig. 6. Fracture at interface pattern after deformation by: (a) TE and (b) HPTE (white arrows indicate cracks appearance).



a



b

Fig. 7. EDX line scan analysis across the (a) aluminium-intermetallic boundary (distance between points is 1 μm) and (b) the copper-intermetallic boundary (distance between points is 5 μm); (lamella for TEM study has been lifted from region indicated by the white box in panel a).

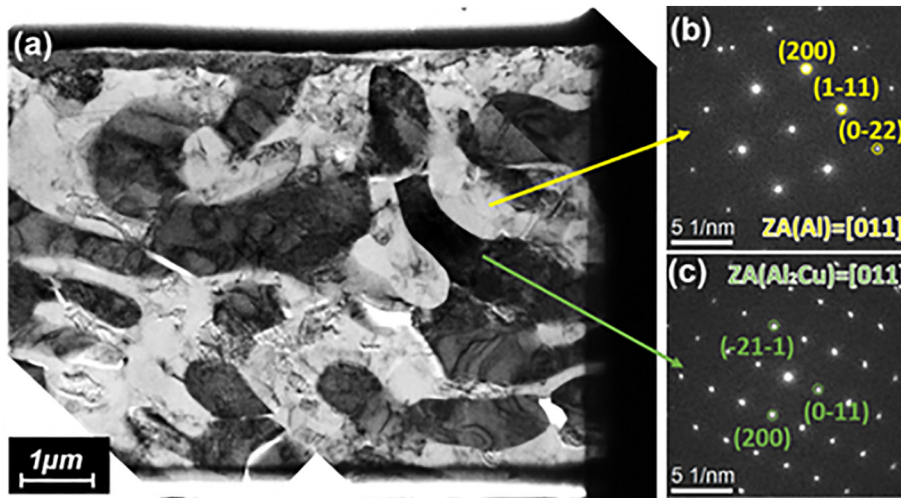


Fig. 8. TEM characterization of the interface zone after deformation by HPTE. (a) BF image; (b) SADP from an Al grain; (c) SADP from an Al_2Cu grain.

sample 11 was measured after casting ($\sim 43.3\%$ IACS) and the average value was much lower than that of pure aluminium casting, which reflects the strong influence of the intermetallic compound with low conductivity. To increase the copper volume fraction gradually, the sample diameter was turned down several times and the conductivity was measured after each turning.

The results of the conductivity measurements are presented by blue points in Fig. 4. It can be seen that the scattering is quite strong, perhaps due to possible fractional misalignment during the turning operation. The fitting line, however, follows the trend and is almost parallel to the theoretical line calculated by the rule of mixture (11).

$$\sigma_{ef} = \sigma_{Al}f_{Al} + \sigma_{Cu}f_{Cu} = \sigma_{Al}(1-f_{Cu}) + \sigma_{Cu}f_{Cu}, \quad (11)$$

The difference between lines can be attributed to the presence of the intermetallic layers with conductivity in the range (4...15)%IACS. More precision can be attained if Eq. (12) is used to calculate the effective conductivity of such composites.

$$\sigma_{ef} = \sigma_{Al}(1-f_{Cu}-f_{Int}) + \sigma_{Cu}f_{Cu} + \sigma_{Int}f_{Int} \quad (12)$$

Comparison of the theoretical curves calculated by Eqs. (11) and (12) shows that they are quite close for small copper volume fractions, given that the volume fraction of the intermetallic compound is proportional to f_{Cu} . Nonetheless, as f_{Cu} increases, the theoretical line, which reflects the presence of the intermetallic phase, Eq. (12), deviates from the line for Eq. (11) and approaches the experimental fitting line, Fig. 4.

The difference between the theoretical and the experimental fitting curves Δ is about 8%IACS. Using Eqs. (11) and (12), this difference can be estimated as:

$$\Delta = f_{Int}(\sigma_{Al} - \sigma_{Int}). \quad (13)$$

As the phase $\theta\text{-Al}_2\text{Cu}$ is the major one in the interface, Fig. 2, we can calculate the intermetallic (IM) volume fraction, using the data in Table 2. The IM fraction turns out to be about $f_{Int} = 0.1538$, which allows us to estimate the average thickness of the interface zone, $\sim 340 \mu\text{m}$, comprising an inter-diffusion layer and intermetallic phase layers.

3.3. Characterization of samples after SPD

In Table 4, the SEM BS images of the cross-sections of samples deformed by three different SPD techniques are presented. For each process, the images in columns show the aluminium, copper and interface regions, respectively. The average grain size collected from the number of SEM images is $d_{Cu} = 380 \pm 120 \text{ nm}$, $210 \pm 80 \text{ nm}$, $160 \pm 150 \text{ nm}$ and $d_{Al} = 14.3 \pm 6.1 \mu\text{m}$, $1.8 \pm 1.2 \mu\text{m}$, $0.46 \pm 0.15 \mu\text{m}$ for samples processed by the RE, TE and HPTE processes, respectively.

It should be noted that the microstructure is extremely non-homogeneous with the presence of very small grains (below 50 nm) within prominent shear bands (mostly in the RE processed samples) and almost undeformed initial large grains of around $200 \mu\text{m}$ alongside the band of ultrafine grains for the TE processed samples. The non-

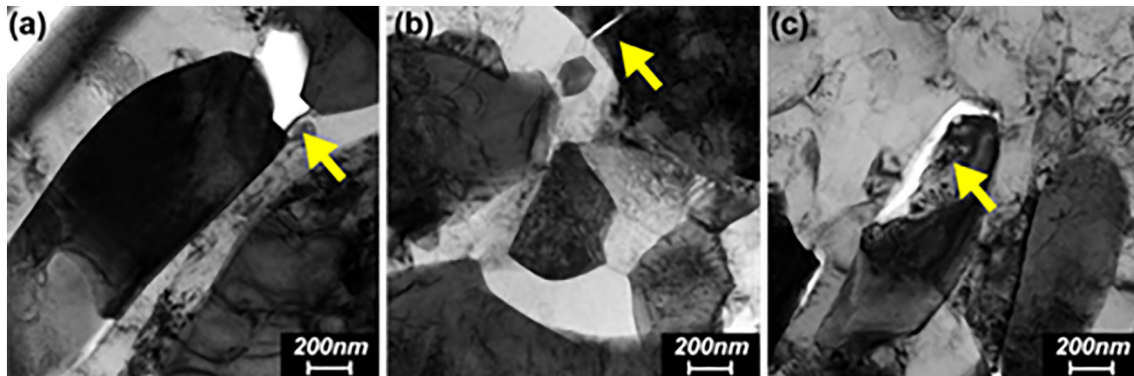


Fig. 9. TEM images of grains in the Al- Al_2Cu intermixing zone after deformation by HPTE and initiation of cracks: (a) between two Al_2Cu grains; (b) within Al_2Cu grain; (c) between Al and Al_2Cu grains (crack initiation indicated by arrows).

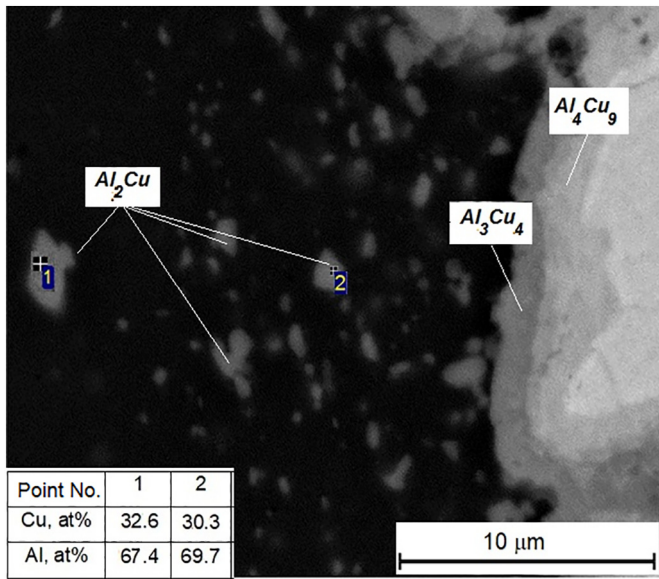


Fig. 10. BS SEM image of interface zone after RE deformation.

uniform distribution of equivalent strain in the cross-section of the TE deformed samples [16] promotes the non-uniformity of the microstructure.

The grain size in the aluminium and copper constituents of the deformed samples is presented as a function of deformation temperature and equivalent strain in Fig. 5. These functions of the two variables show that d_{Al} is more dominated by the processing temperature than d_{Cu} , on which the equivalent strain has the main effect. In the last row of Table 4, the images of the interface between Al/Cu are shown after each deformation process. It can be seen that only the RE deformed samples maintain the integrity of the interface zone. For the other two processes, constituents are separated by cracks propagating through the brittle intermetallic phases. Multiple cracks appear in the HPTE deformed samples due to the lower deformation temperature.

Analysis of the interface zone after HPTE and TE processing shows the presence of the same phases as in the initial as-cast state, Figs. 2 and 3. These phases are quite brittle at low temperatures [21,23], evidenced by their damage during plastic deformation. After TE, a single crack propagating through the θ -Al₂Cu phase is seen clearly in Fig. 6a, while multiple cracks were observed within all three θ -Al₂Cu, ζ -Al₃Cu₄ and γ -Al₄Cu₉ phases, Fig. 6b. These multiple cracks, parallel and perpendicular to the phase boundaries, develop during SPD, are introduced by HPTE in comparison to mid-level strain introduced by TE.

The intermetallic phase was defined by EDX line scan analysis across the aluminium-intermetallic and copper-intermetallic boundaries, with results shown in Fig. 7. A mixture of the two-phase Al₂Cu and Al(Cu) solid solution creates a 200 μm wide zone, and has a lamella morphology with spacing of 300–400 nm. This is followed, moving toward the copper, by a 2–10 μm-wide Al₃Cu₄ zone and an approximately 5 μm-wide Al₄Cu₉ zone.

The microstructure refinement and crack initiation due to HPTE processing were analysed by TEM, Figs. 8 and 9. As seen in Fig. 8a, full intermixing of the Al₂Cu phase and Al matrix due to fragmentation of the brittle intermetallic phase is observed. The extensive grain refinement can be seen in both the Al matrix and the Al₂Cu phase, Fig. 9. The redistributed Al₂Cu grains have very close crystallographic orientations and exhibited a similar diffraction contrast as what is observed in Fig. 8a. The grain rotation was restricted due to the low temperature, which led to crack initiation between intermetallic grains, Fig. 9a, b, as well as between intermetallic and matrix grains, Fig. 9c.

It should be noted, that the average Al grain size after HPTE is shown to be 460 ± 150 nm estimated from SEM characterization (Table 4), while it looks twice smaller from TEM images. This is explained by the difference in the intensity of grain refinement in the Al matrix at the distance from interface and in the vicinity of interface. In proximity of interface more severe grain-refinement takes place. It is generally accepted that in co-deformation of two materials, the softer phase (Al) flows around harder phase (Al₂Cu) and experiences higher strain. Therefore, more extensive grain refinement of Al is observed in the intermixing zone.

Analysis of the interface after RE revealed a completely different situation, Fig. 10. Apparently, the biggest θ -Al₂Cu phase has been dissolved due to SPD (~1000%) under high hydrostatic pressure and high

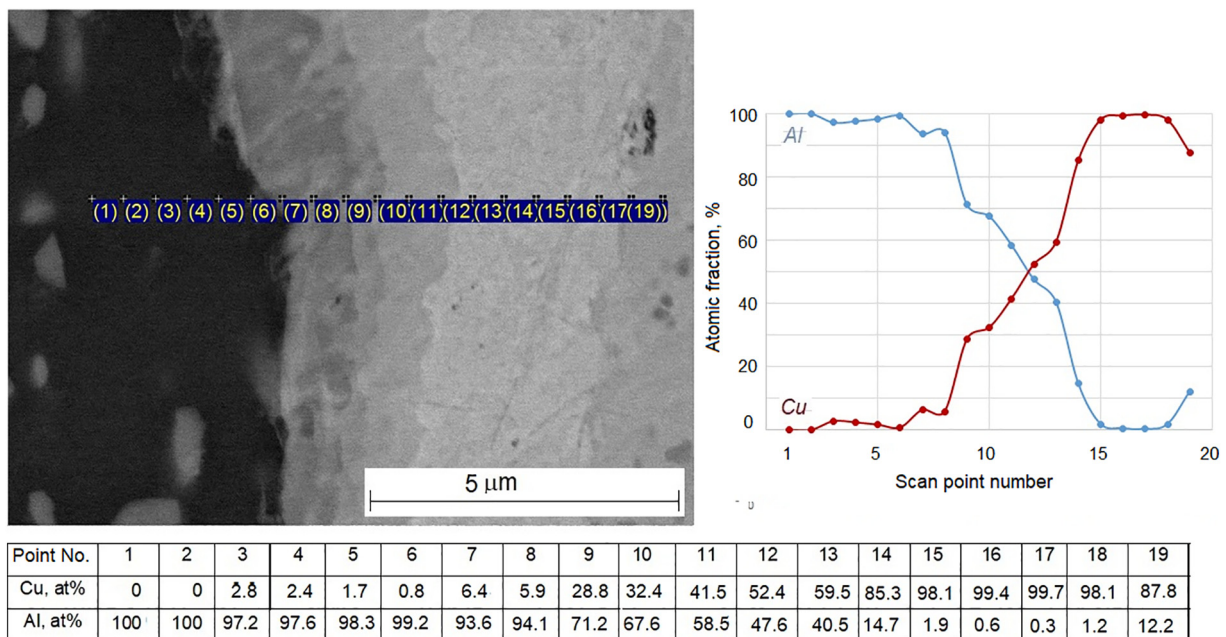


Fig. 11. BS SEM image with EDX line scan analysis across interface after RE deformation (distance between points is 0.5 μm).

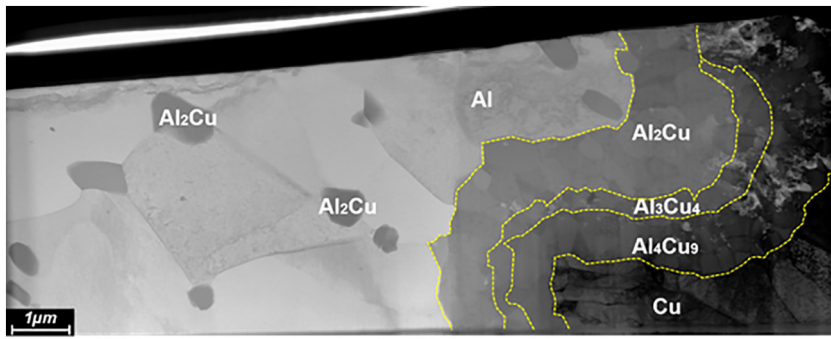


Fig. 12. STEM-DF characterization of the interface zone after deformation by RE.

temperature (400 °C). Only small particles of this phase remained. The other two phases were partially dissolved and the interface width has been reduced to about 3–5 μm, as can be seen in Fig. 11.

In addition to a drastic reduction in the interface zone width (50 times smaller), the intermetallic phases reached sufficient ductility at 400 °C and extensive grain refinement was observed within the intermetallic layers, Fig. 12. The average grain size of intermetallic phases Al_2Cu , Al_3Cu_4 and Al_4Cu_9 was 530 ± 171 nm, 313 ± 114 nm and 372 ± 152 nm, respectively. Therefore, it is expected that RE process will be the optimal method for simultaneously increasing strength and conductivity for structures comprising copper helices inserted within aluminium cast billets and subjected to SPD.

Other methods to govern the thickness of interface between aluminium and copper are discussed in [25]. It was shown by experiments that the thickness of the interlayer clearly correlates with the friction-stir welding process temperature. Therefore, the other methods are available to create the hybrid conductors with helical architecture.

3.4. Electrical conductivity of samples after SPD

Samples 1–10 (Table 2) with different helices covering the region of the copper volume fraction up to a maximum of 0.152 were subjected to three different SPD processes. Electrical conductivity measured before and after deformation versus the copper volume fraction is presented in Fig. 13a. Electrical conductivity measured after deformation and annealing at 250 °C for 4 h is presented in Fig. 13b.

The electrical conductivity values before deformation (black curve, Fig. 13a) are quite close to the experimental values shown in Fig. 4 for sample 11 (in the same range of f_{Cu}). After deformation by TE where the accumulated strain is relatively small (30–120%) and the temperature is relatively high (200 °C), conductivity improves due to the closing of casting defects and elimination of the sample's dendritic structure. The more severe plastic deformation by RE (up to 1000%) results in a decrease in electrical conductivity even though the processing was done at a high temperature (400 °C). A significant drop in conductivity was observed after deformation by HPTE, which applied a high level of strain (930%) at room temperature. We note that for all samples except those processed by HPTE, the conductivity has a strong linear dependence on the copper volume fraction. Considering the inclination angle of fitting lines, it could be noticed that RE and RE - annealed samples have the steepest increase of conductivity with increase of copper volume fraction. The conductivity of these samples exceeds conductivity of samples deformed by other SPD processes, when f_{Cu} reaches the value of 0.16 and has the tendency to saturate for higher values of f_{Cu} . It can be seen that annealing at 250 °C improves the conductivity but the tendency remains. To understand the nonlinear character of the 'conductivity versus copper volume fraction' function, the continuity of the copper helix was checked by XT tomography.

3.5. Continuity of copper helix after SPD

The 3D reconstructed images of samples after SPD are shown in Fig. 14. These images confirm that the RE and TE processes do not disrupt the copper helices, Fig. 14a, b, whereas HPTE breaks the helix into small fragments, Fig. 14c. The effect of randomly distributed copper fragments on conductivity cannot be described by the analytical model

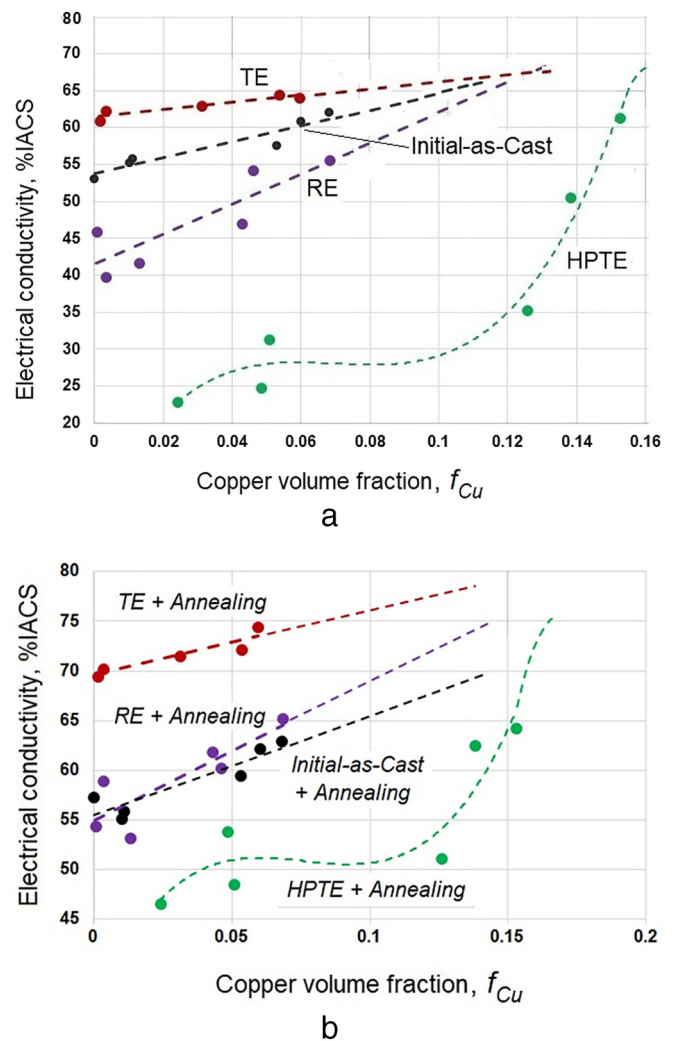


Fig. 13. Electrical conductivity of the samples versus copper volume fraction. (a) Before and after deformation by TE, RE, and HPTE; (b) after deformation and annealing at 250 °C for 4 h.

developed for continuous helices and presented in Section 4.1. Therefore, the model for HPTE processed samples is discussed separately in Section 4.2.

3.6. Compression behaviour of hybrid samples

All samples underwent compression testing in its original shape. Samples after TE and RE processing were tested only to a few percent of plastic strain (7–10%) above yield given that their dimensions were very big and the load exceeded the Instron capacity. Samples after HPTE and RE cut from material in the neck of the hourglass die (designated further as RE-s) were tested to the full range of plastic strain. The results were consistent with the prediction of the model developed in [26]. This model predicts that hybrid samples with helical reinforcement exhibit higher yield strength, increased load-bearing capability

and higher stiffness due to nonlinear behaviour of the spring embedded in the matrix compared to linear reinforcement of the matrix, Fig. 15. The theoretical linear model, based on the rule of mixture (dashed line in Fig. 15), predicts much lower values of yield stress for our hybrid samples than displayed by our experimental results, shown by round symbols. It should be noted that yield stress for aluminium and copper in the theoretical linear model were taken correspondingly to the strain level and temperature of deformation for each process. The inserts in Fig. 15 demonstrate the engineering stress–strain curves for the biggest volume fraction of copper in each process tested to 7–10% of plastic strain. Therefore, the strain hardening parameter could not be defined for samples TE and RE, though visually strain hardening is bigger for RE samples.

Samples, after HPTE and RE-s, were tested over the full range of plastic strain where the expected tendency of enhanced strain hardening

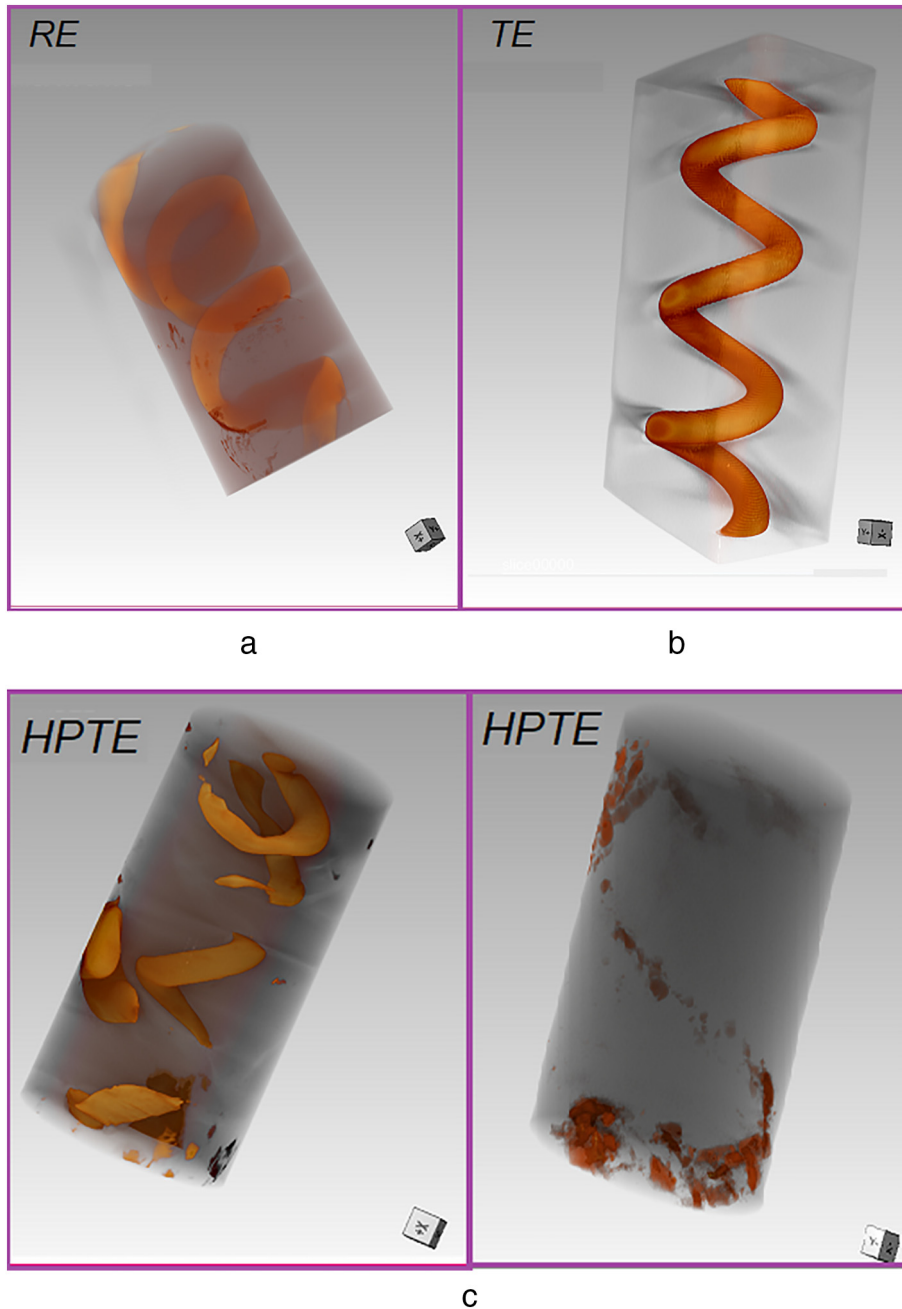


Fig. 14. XR tomography images of samples after deformation by (a) RE; (b) TE; (c) HPTE (left image – rod 2, right image – rod 1).

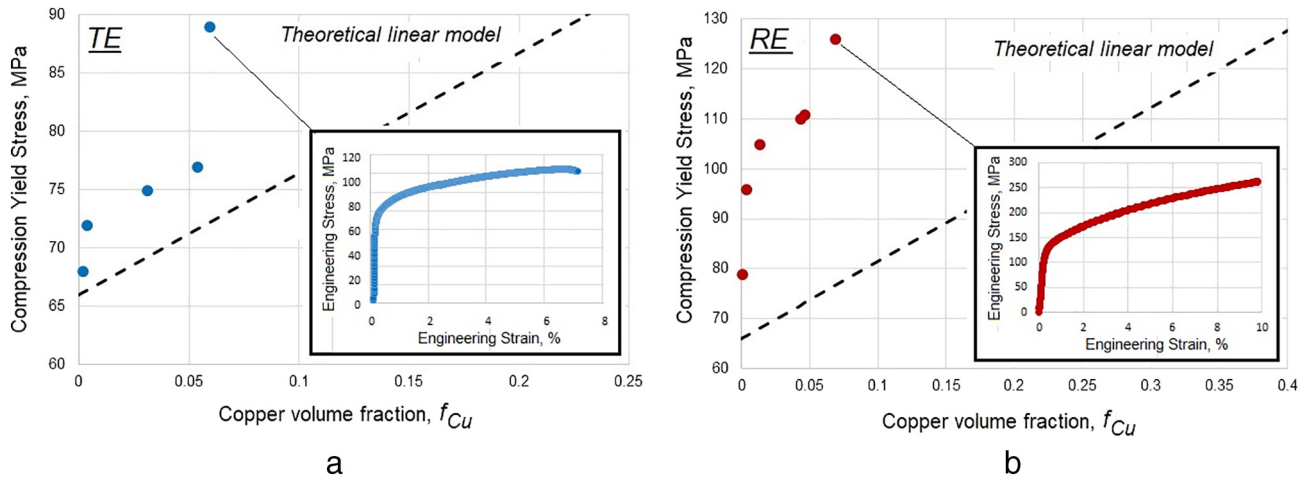


Fig. 15. Yield stress in compression for samples deformed by: (a) TE; (b) RE.

was observed. Some representative curves compared to the stress-strain curve for annealed CP Al are shown in Fig. 16. A higher slope was observed for hybrids with higher volume fractions of copper. A comparison of the two curves for HPTE ($f_{Cu} = 0.051$) and RE ($f_{Cu} = 0.045$) processed samples with similar copper volume fractions, however, shows higher effective strain hardening ($n = 0.46$) for the RE-s samples than for the HPTE sample ($n = 0.34$). This result can be explained by the difference in parameter introduced by Bouaziz in [27], which actually is the winding diameter-to-pitch ratio of the helix (D/p). The small number of samples available for testing over a full range of plastic strain restricted the definition of effective strain hardening as a function of two parameters— f_{Cu} and D/p . Nevertheless, the difference in the compressive behaviour and the effective strain hardening parameter is clearly seen in Fig. 16.

It is expected that spiral reinforcement of materials will demonstrate the benefits of such hybrid architectures for tensile loading as well. The benefits due to postponing of the necking onset and increased tensile ductility [26] should also make this technique attractive.

4. Theoretical model of the effective electrical conductivity of hybrid materials

Many theoretical models for prediction of effective electrical conductivity of composite materials were developed during the 20th century and comprehensive reviews of these can be found, for example,

in [28]. The two most common approaches were percolation theories and effective media theories, and they were used until McLachlan proposed the general effective media (GEM) model, combining the main features of both approaches [29]. In his model, the effective conductivity of composite material with two constituents depends not only on conductivity and volume fraction of each component but on their shape and interconnectivity.

The model of effective conductivity, σ_{ef} , for hybrid samples with one constituent possessing a helical internal architecture was developed and presented in Section 4.1. It was assumed that the distance L between two probe points is significantly larger than the pitch of the helix p and the effective conductivity is the inverse value of electrical resistivity defined by formula (4). The model was developed for hybrid materials with a continuous copper wire, such as our samples, deformed using RE and TE processes, while for samples deformed by HPTE, McLachlan's model [29] was applied.

4.1. Models of electrical conductivity of hybrid samples with a helical internal architecture

The model is derived under the assumption that the current runs parallel to the sample axis (for similar resistivity of constituents). The situation in which the current runs along the copper helix only (resistivity of aluminium is very high, close to dielectric) is not realised.

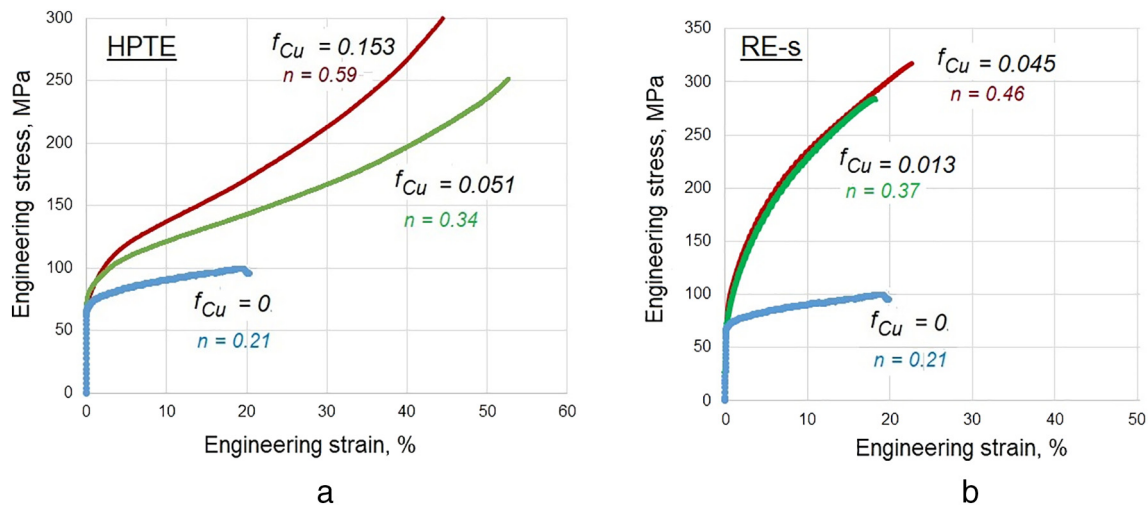


Fig. 16. Engineering stress-strain curves resulting from compression of the samples deformed by: a - HPTE; b - RE (cut from material in the neck of the hourglass die).

The model regards a sample with a continuous helix as two conductors connected in parallel, Fig. 5a. The first conductor is a hollow cylinder (I) of diameter D ($D = 2R$ is the winding diameter) and wall thickness d ($d = 2r$ is the wire diameter), which contains the copper helix. It has a base area equal to:

$$S^I = \frac{\pi((D+d)^2 - (D-d)^2)}{4} = \pi Dd \quad (14)$$

The second conductor is an aluminium cylinder (II) having the volume remaining after subtraction of the hollow cylinder's volume, Fig. 17a. Both conductors should have the same height and, therefore, the base area of the aluminium cylinder (II) is: $S^{II} = S - S^I$, where S is the base area of the hybrid sample.

Here we introduce a parameter,

$$f'_{Cu} = \frac{S^I}{S} = \frac{\pi Dd}{S}, \quad (15)$$

which characterizes the volume fraction of the cylinder (I) in the hybrid sample.

The presentation of the hybrid sample as two cylinders leads to the assumption of their connection in parallel. To calculate the effective conductivity per helix pitch, we consider one layer of height p .

Designating the conductivities of cylinders (I) and (II) by $\bar{\sigma}^I$, $\bar{\sigma}^{II}$, respectively, first we calculate the conductivities using the schematic presented in Fig. 17b, c. Then we use the additivity of the conductivities for in-parallel connection of the conductors.

Each layer of cylinder (I), Fig. 17b, consists of a set of columns (with width Δ , thickness d and height p) connected in parallel, where each column has two aluminium parts, two interfaces and one copper part connected in series.

Therefore, the electrical resistance of each column is equal to:

$$r = \frac{h_{Al}}{d \cdot \Delta \cdot \sigma_{Al}} + \frac{h_{Cu}}{d \cdot \Delta \cdot \sigma_{Cu}} + \frac{2\delta}{d \cdot \Delta \cdot \sigma_{Int}}. \quad (16)$$

here h_{Al} , h_{Cu} and δ are the effective heights of the aluminium, copper and interface parts within one column, respectively.

The conductivity of the hollow cylinder (I), Fig. 17b, is calculated by summation of all the columns' conductivities:

$$\begin{aligned} \bar{\sigma}^I &= \sum r^{-1} = \sum d \cdot \Delta \cdot \left(\frac{h_{Al}}{\sigma_{Al}} + \frac{h_{Cu}}{\sigma_{Cu}} + \frac{2\delta}{\sigma_{Int}} \right)^{-1} \\ &= S^I \left(\frac{h_{Al}}{\sigma_{Al}} + \frac{h_{Cu}}{\sigma_{Cu}} + \frac{2\delta}{\sigma_{Int}} \right)^{-1}. \end{aligned} \quad (17)$$

The conductivity of the aluminium cylinder (II) with the same height p is equal to:

$$\bar{\sigma}^{II} = \frac{\sigma_{Al}(S - S^I)}{p}. \quad (18)$$

Therefore, the effective conductivity of the whole sample can be written as:

$$\sigma_{ef} = \bar{\sigma}^I + \bar{\sigma}^{II} = \frac{\sigma_{Al}(S - S^I)}{p} + S^I \left(\frac{h_{Al}}{\sigma_{Al}} + \frac{h_{Cu}}{\sigma_{Cu}} + \frac{2\delta}{\sigma_{Int}} \right)^{-1}. \quad (19)$$

Considering that the thickness of the intermetallic is negligibly small ($2\delta \ll h_{Cu}$), the final expression of effective conductivity can be written as:

$$\sigma_{ef}(f'_{Cu}, f''_{Cu}) = \sigma_{Al}(1 - f'_{Cu}) + f'_{Cu} \frac{1}{\frac{f''_{Cu}}{f'_{Cu}} \sigma_{Cu}^{-1} + (1 - f''_{Cu}) \sigma_{Al}^{-1} + k f''_{Cu} \sigma_{Int}^{-1}}, \quad (20)$$

where

$$f''_{Cu} = \frac{h_{Cu}}{p} \quad (21)$$

is the volume fraction of copper in the cylinder (I), Fig. 17, and $k = 2\delta/h_{Cu}$.

Model, based on the rule of mixture, depend only on one parameter: the volume fraction of copper, f_{Cu} , in a whole sample. Our model, on the other hand, rests on two independent parameters: (i) f'_{Cu} , which characterises the volume of the hollow cylinder containing the helix and (ii) f''_{Cu} , which characterizes the volume of copper within the helix-confining hollow cylinder. Actually, f_{Cu} is decomposed into two additional parameters according to the following expression:

$$f_{Cu} = f'_{Cu} \cdot f''_{Cu}. \quad (22)$$

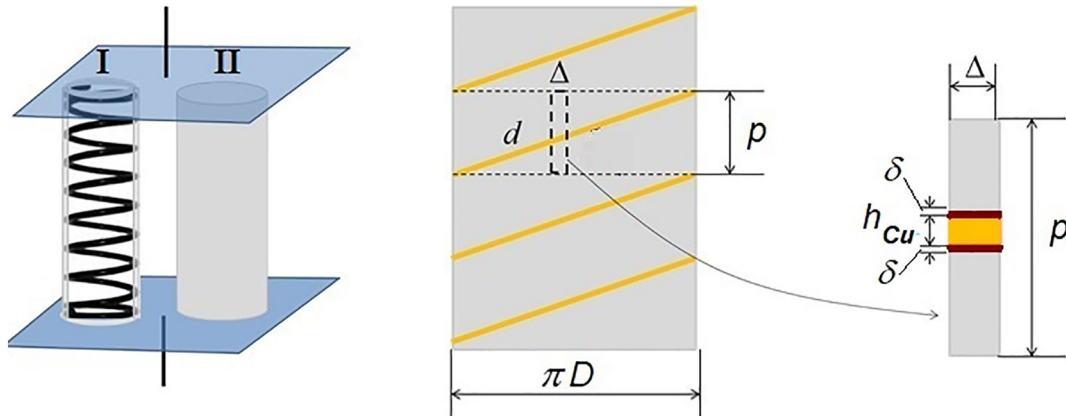


Fig. 17. Illustration of the electrical resistance model for hybrid material with one helix constituent. (a) Schematic of helix and matrix connected in parallel; (b) 2D hollow cylinder surface representation; (c) enlargement of one column.

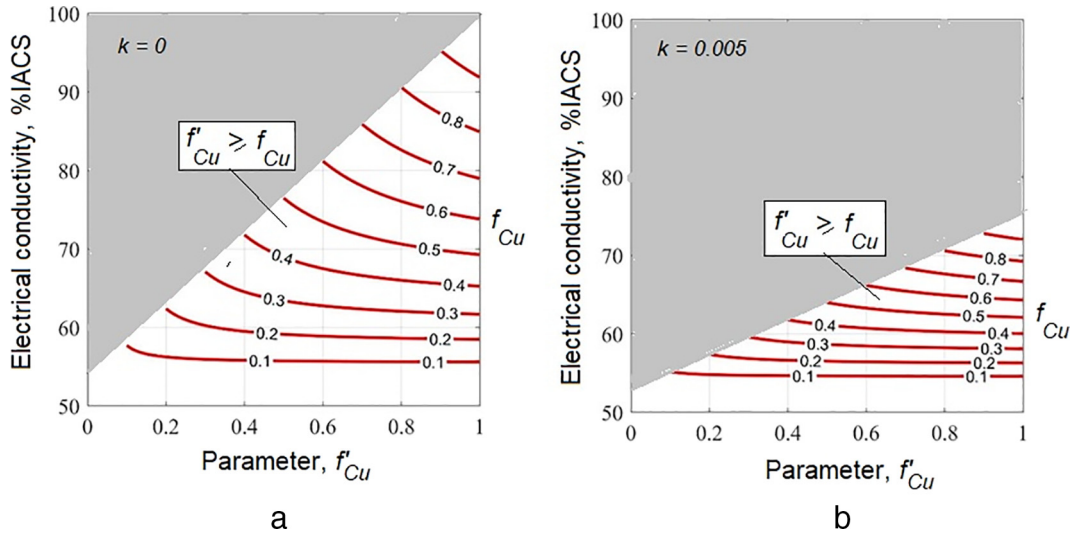


Fig. 18. Maps of $\sigma_{ef}(f_{Cu}, f'_{Cu})$ for: (a) $k = 0$; and (b) $k = 0.005$. (Eq. (23) is not satisfied within the grey shadowed area.)

Obviously, the following limitation is valid:

$$0 \leq f_{Cu} \leq f'_{Cu} \leq 1. \tag{23}$$

For convenience, Eq. (20) can be re-written as a function of f_{Cu} and f'_{Cu} :

$$\sigma_{ef}(f_{Cu}, f'_{Cu}) = \sigma_{Al}(1-f'_{Cu}) + (f'_{Cu})^2 \frac{1}{f_{Cu}(\sigma_{Cu}^{-1} + k\sigma_{int}^{-1}) + (f'_{Cu} - f_{Cu})\sigma_{Al}^{-1}}. \tag{24}$$

Eq. (24) was used to draw the maps of effective electrical conductivity. The examples of the maps representing function $\sigma_{ef}(f_{Cu})$ for different fixed levels of f_{Cu} and the two different parameters of k —(i) $k = 0$ (absence of intermetallic); and (ii) $k = 0.005$ (thin layer of intermetallic 7.5–12.5 μm)—are shown in Fig. 18a, b. From Eq. (23), it is obvious that the map values should be considered only in the non-shadowed area, $f_{Cu}' \geq f_{Cu}$.

The maximum value of $\sigma_{ef}(f_{Cu}') = \sigma_{ef}^{max}$ is reached when $f_{Cu}' = f_{Cu}$ and is equal to:

$$\sigma_{ef}^{max} = \sigma_{Al}(1-f_{Cu}) + \sigma_{Cu} \frac{f_{Cu}}{\left(1 + k \frac{\sigma_{Cu}}{\sigma_{int}}\right)}. \tag{25}$$

From Eq. (24), it can be seen that the maximum effective conductivity is reached when the copper volume fraction is close to 1, which is obtained when the pitch value goes to zero and the hollow cylinder (I) comprises only copper or, in other words, the hollow cylinder (I) is a copper tube.

It should be noted that at $k = 0$, Eq. (23) is transformed into Eq. (11), which calculates the effective conductivity by the rule of mixture. For the general case of $k \neq 0, f_{Cu}' \neq f_{Cu}$, however, our model takes into account the presence of intermetallic phases and all constituent connections, in parallel and in series, which are represented by Eq. (24). Clearly, the value of effective conductivity also depends on three constituent conductivities, which change with the level of strain.

The maps in Fig. 18 show that effective conductivity generally increases with the volume fraction of copper f_{Cu} , but for each fixed value of f_{Cu} , it slightly decreases as the parameter f_{Cu}' increases. Considering

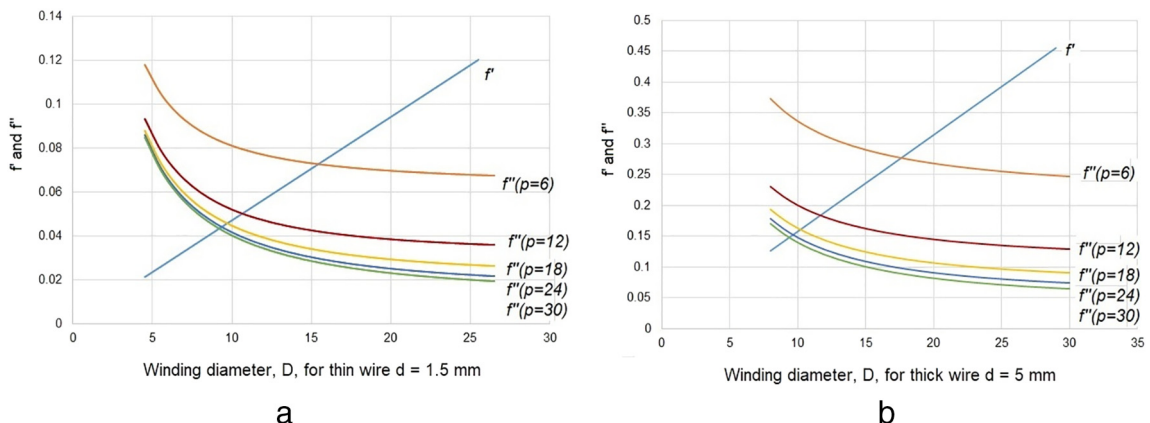


Fig. 19. Parameters f_{Cu}' and f_{Cu}'' vs. winding diameter for five different pitch values (6, 12, 18, 24 and 30 mm): (a) thin ($d = 1.5$ mm) wire; (b) thick ($d = 5$ mm) wire.

Table 5

Values of model parameters for samples subjected TE and RE processing.

	TE				RE			
f_{Cu}	0.0015	0.0536	0.0594	0.0311	0.0034	0.0034	0.0428	0.0684
f_{Cu}'	0.0778	0.2356	0.2356	0.1414	0.0542	0.0808	0.3265	0.3265
f_{Cu}''	0.0193	0.2275	0.2521	0.2199	0.0627	0.0421	0.1311	0.2095
k	0.33	0.1	0.1	0.1	0.33	0.0067	0.002	0.002

Eq. (22), the effective conductivity should increase as parameter f_{Cu}'' increases. Theoretically, this parameter can be calculated as:

$$f_{Cu}'' = \frac{f_{Cu}}{f'} = \frac{d}{4D} \sqrt{1 + \frac{(D+d)^2}{p^2}}, \quad (26)$$

and, therefore, parameter f_{Cu}'' depends on all three helix parameters: winding diameter – D , wire diameter – d and helix' pitch – p .

Plotting both parameters, f_{Cu}' , f_{Cu}'' (Eqs. (15) and (26), Fig. 19), the following trends can be observed:

- (i) f_{Cu}'' decreases exponentially with the winding diameter;
- (ii) f_{Cu}'' decreases with pitch size for both wire diameters, though to a higher degree for thick wire;
- (iii) f_{Cu}' increase linearly with the winding diameter and does not depend on pitch size;
- (iv) the product of f_{Cu}' and f_{Cu}'' , representing the copper volume fraction (Eq. (22)), is the biggest for small pitch sizes and big winding diameters.

To validate the model, parameters of samples subjected to TE and RE processing (see Table 5) were substituted into Eq. (24) and σ_{ef} was calculated and compared to conductivity measured in the experiments, Fig. 13a, b. The correlation coefficient between theoretical prediction and experimental data was 0.884, Fig. 20.

The developed analytical model is instrumental in the analysis of the contribution of different architecture parameters to effective conductivity of hybrid conductors. Obviously, an increase in the copper volume fraction f_{Cu} results in higher conductivity of the hybrid material, while an increase in the intermetallic volume fraction leads to the opposite effect. The f_{Cu} increase could be achieved by increasing the wire diameter and/or the winding radius and by decreasing the helix pitch. Nevertheless, despite the thickness of the intermetallic compound δ , which depends only on manufacturing and deformation methods, all these parameters define the intermetallic compound volume fraction.

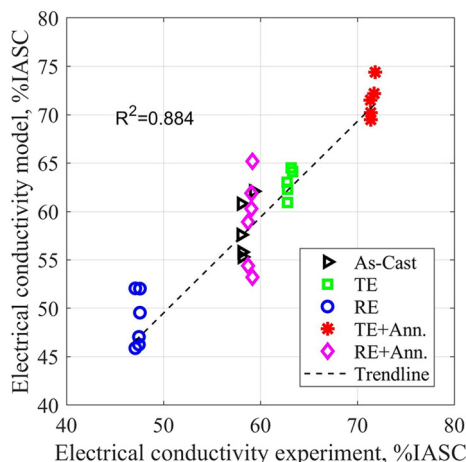


Fig. 20. Effective electrical conductivity: Model prediction versus experimental data.

For example, we consider two aluminium cylindrical samples 35 mm in diameter, with incorporated copper helixes 15 mm and 25 mm in winding diameter, respectively. If the helix is made from a thick wire 5 mm in diameter, then parameter f_{Cu}' , from Eq. (15) is equal to 0.3265 and 0.4898 for the first and second cylinder, respectively. For a helix made from a thin wire 1.5 mm in diameter, parameter f_{Cu}' is equal to 0.081 and 0.1298 for the first and second cylinder, respectively. Fig. 21 shows the effective conductivity, calculated using Eq. (24), for these two cases and intermetallic layers 150 μm and 250 μm wide. Parameter k introduced in Eq. (24) takes the value of 0.06 and 0.1 for a thick wire and 0.2 and 0.33 for a thin wire. It can be seen that two competitive processes are present. For the same wire diameter, if the intermetallic layer is 250 μm wide, the conductivity decreases, but for an intermetallic layer of 150 μm wide, the conductivity increases. Therefore, the volume fraction of copper increases the effective conductivity while the intermetallic layer formed on the interface causes it to decrease. To obtain a steady increase in effective conductivity, the interface width should be reduced ($k \rightarrow 0$), while the volume fraction of cylinder (I) within the sample should increase.

The developed model could be used to design Al–Cu hybrid conductors, benefitting from the high strength and high conductivity of copper and the lightweight of aluminium. In Fig. 22, the effective conductivity calculated using our model (Eq. (24)) versus the specific weight of Al/Cu conductor is plotted. Four regions shown in this plot represent conductors made from aluminium with $\sigma_{Al} = 66\% \text{ IACS}$ (regions I and II) and with $\sigma_{Al} = 53\% \text{ IACS}$ (regions III and IV), while the conductivity of copper was always 100%IACS. The green point represents the average conductivity of aluminium between the two limiting cases considered. For regions I and III, $k = 0$ (no intermetallic forms), while for regions II and IV, $k = 0.05$ (the thickness of the intermetallic layer is about 125 μm). It can be seen that for $k = 0$, both regions I and III reach a value close to the copper level, but for $k = 0.05$, regions II and IV have different inclination angles and reach a much lower maximum conductivity. The dots within each region represent different geometrical parameters of the helix, which can be varied to optimise the specific weight at the same level of effective conductivity (within the width of the region) or to optimise the effective conductivity at a pre-set specific weight (within the height of the region). An example of possible design variations is indicated by the dashed line intersecting the point with $\sigma_{ef} = 80\% \text{ IACS}$ and a specific weight of $50^{kN} / m^3$.

4.2. Models of electrical conductivity of hybrid samples with a disrupted helical constituent

As mentioned already at the beginning of Section 4, the interconnectivity of each constituent is extremely important. We saw that the mechanical turning of samples for HPTE processing followed by SPD at room temperature resulted in disruption of the copper helix. The modelling of aluminium samples with copper/intermetallic inclusions can be analysed by McLachlan's GEM equation in general form:

$$f_{Al} \cdot \frac{(\sigma_{Al}^{1/t} - \sigma_{ef}^{1/t})}{\sigma_{Al}^{1/t} + A\sigma_{ef}^{1/t}} + f_{Cu} \cdot \frac{(\sigma_{Cu}^{1/t} - \sigma_{ef}^{1/t})}{\sigma_{Cu}^{1/t} + A\sigma_{ef}^{1/t}} = 0, \quad (27)$$

where t, A are two parameters of the model that account for the geometry, interconnectivity and critical percolation volume fraction of the constituent with higher conductivity.

It is shown in [27] that for a symmetrical lattice model, parameter A can be expressed via the critical percolation volume fraction of the high conductivity phase, $A = f_c / (1 - f_c)$. Nonetheless, as discussed in [29], when fitting Eq. (27) to experimental data, different values of parameter A could appear, compared to those predicted by percolation theory ($f_c \approx 0.16 \approx 0.19$); and the value of f_c could change for symmetrical and random lattices from 0.02 to 0.6 of the volume fraction.

It should be noted that there is not enough experimental data to find the best fit of McLachlan's GEM Eq. (27). By fitting the left group of points with an exponential function and the right group of points with a logarithmic function, however, we can define the percolation threshold to be approximately around 0.1 (dashed line in Fig. 23). The values in the vicinity of the threshold on the right side represent the case of the conductive constituent being embedded in a non-conductive matrix, while the values on the left side in the vicinity of the threshold represent the case of infinite conductivity of constituents embedded in the matrix. Fitting the experimental data to the effective conductivity curve obtained from Eq. (27) (black line in Fig. 23) gives the value of the fitting parameters $f_c = 0.0877$ $t = 0.09$, though the small number of points cannot provide reliable results and should only be used to indicate a direction for further research on aluminium conductors with disrupted copper constituents.

5. Conclusions

- To leverage the benefits of copper's high strength and high conductivity and aluminium's lightweight, Al—Cu hybrid conductors could be designed. The novel design was suggested in the present work. The copper constituent was used as a helical wire fully embedded in the aluminium matrix. The interdiffusion at the interface between aluminium matrix and copper helix during casting results in formation of interfacial intermetallic phases. Three phases of different thicknesses were observed: θ -Al₂Cu, ζ -Al₃Cu₄ and γ -Al₄Cu₉.
- It was confirmed that hybrid samples with helical reinforcement exhibit higher yield strength, increased load-bearing capability and higher strain hardening during deformation than predicted by rule of mixtures. Samples with very small volume fractions of copper (~0.05) exhibited quite high strain hardening exponents ($n = 0.34$ – 0.46) compared to that typical of aluminium, $n \approx 0.2$.
- The SPD processing method was shown to be important for strengthening of the hybrid due to grain refinement within constituents and within intermetallic layers. The SPD processes employed in this work and conducted at low temperature and with insufficient hydrostatic pressure, however, resulted in fracture of brittle interfacial intermetallic compounds and separation of constituents in the hybrid samples. Moreover, it was shown that very high strains introduced at room temperature, which led to disruption of the helical component, could be beneficial for further increase the electrical conductivity of the hybrid material based on the percolation theory prediction. This phenomenon should be investigated further.
- It was found, that at elevated temperatures and under high hydrostatic pressure, a significant thinning of the interface intermetallic zone was observed. This occurred because of dissolution of the θ -

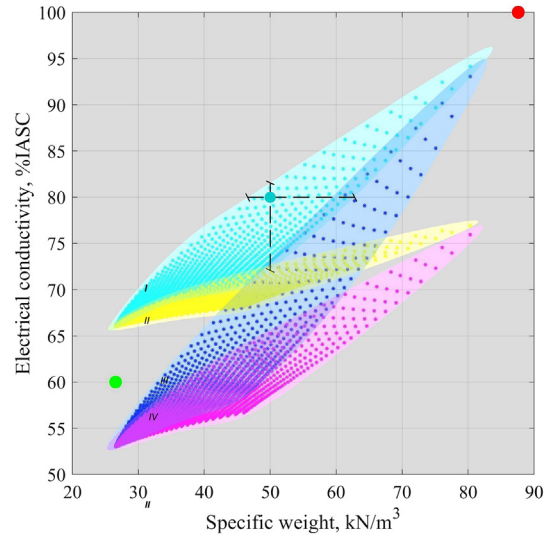


Fig. 22. Effective conductivity (theoretical, Eq. (24)) versus specific weight of the Al—Cu conductor. (I, II - $\sigma_{Al} = 66$ % IACS, $\sigma_{Cu} = 100$ % IACS; III, IV - $\sigma_{Al} = 53$ % IACS, $\sigma_{Cu} = 100$ % IACS; I, III - $k = 0$; II, IV - $k = 0.05$).

Al₂Cu phase, followed by formation of precipitates of similar composition. Therefore, the tailoring of interfacial zone could be done by optimisation of SPD processing.

- It was shown that annealing at 250 °C for 4 h resulted in improvement of conductivity due to recovery of dislocation and relaxation of the micro-stresses at the interface.
- A new analytical model to predict the effective electrical conductivity of hybrid samples was developed. The model takes into account the presence of an intermetallic layer, both in series and in parallel connections of the hybrid's constituents. Contrary to the rule of mixtures, the model depends on two parameters, the product of which represents the volume fraction of copper. Each parameter is determined by the geometry of the helical constituent. The model showed good correlation of the predicted values with the experimental data and can be used for optimal design of hybrid conductors.
- In the case of disruption of the helical constituent by SPD, the effective conductivity could not be described using the developed model. The results were analysed using McLachlan's GEM equation. It should be noted that electrical conductivity growing nonlinearly with the copper volume fraction can potentially generate a sharp increase in conductivity at small volume fractions of copper. Moreover, the alignment of copper fragments along helix shapes results in improved

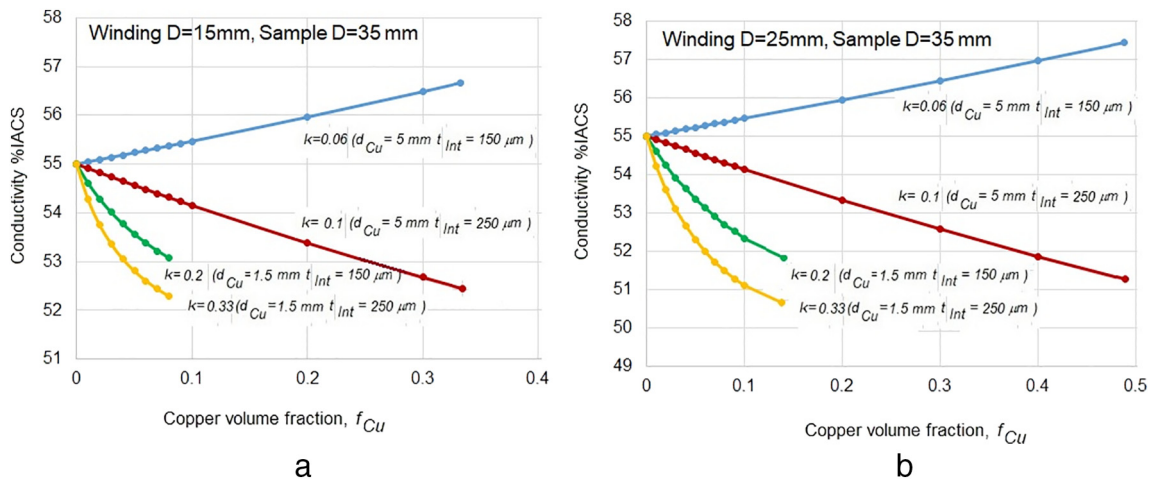


Fig. 21. Effective conductivity of hybrid samples (diameter 35 mm) vs. copper volume fraction for two different winding diameters of the helix: (a) 15 mm; (b) 25 mm.

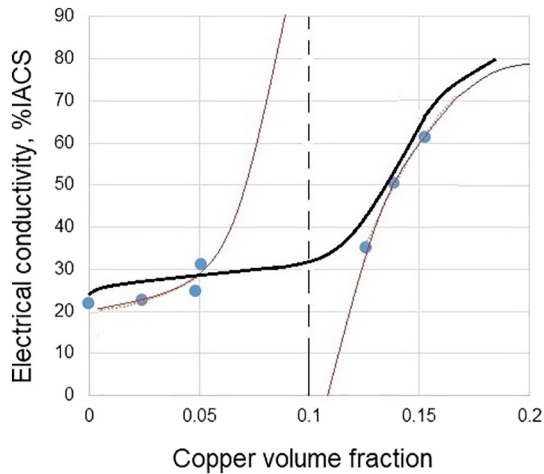


Fig. 23. Analysis of experimental data for HPT processed samples (black line shows the fit to the experimental data using McLachlan's GEM Eq. (27)).

strain hardening of the hybrid, similar to an intact spiral embedded in an aluminium matrix.

- Finally, this work demonstrates that an optimal combination of mechanical strength and electrical conductivity of the helical aluminium-copper hybrids can be achieved by an appropriate selection of the SPD mode and subsequent heat treatments. In particular, the reciprocal extrusion at elevated temperatures has a high potential in reducing the thickness of brittle intermetallic phases formed at the interface during casting, and preserving the morphology and integrity of the copper helices.

CRedit authorship contribution statement

R. Lapovok: Conceptualization, Formal analysis, Writing - original draft. **V.V. Popov:** Formal analysis. **Y. Qi:** Formal analysis, Writing - original draft. **A. Kosinova:** Formal analysis, Writing - original draft. **A. Berner:** Formal analysis, Writing - original draft. **E. Rabkin:** Formal analysis. **R. Kulagin:** Formal analysis, Writing - original draft. **J. Ivanisenko:** Formal analysis, Writing - original draft. **B. Baretzky:** Formal analysis, Writing - original draft. **O.V. Prokofeva:** Formal analysis. **A.N. Sapronov:** Formal analysis. **D.V. Prilepo:** Formal analysis. **Y. Beygelzimer:** Formal analysis.

Declaration of competing interest

The authors declare that they have no known competing financial interests or personal relationships that could have appeared to influence the work reported in this paper.

Acknowledgments

R. Lapovok acknowledges the Marie Curie Fellowship within the EU Framework Programme for Research and Innovation H2020 (Grant - 742098).

The technical help provided by Drs. O. Perroud and Y. Zhao (LEM3 Laboratory, Metz, France) in the X-ray tomographic measurements is greatly acknowledged.

Data availability statement

The raw/processed data required to reproduce these findings cannot be shared at this time as the data also forms part of an ongoing study.

Appendix A. Supplementary data

Supplementary data to this article can be found online at <https://doi.org/10.1016/j.matdes.2019.108398>.

References

- [1] <https://www.kupferinstitut.de/en/materials/application/e-power/conductor-materials.html> 2019.
- [2] Mark Walker (Ed.), Aluminum Electrical Conductor Handbook, 3d edition Aluminium Association, 1989.
- [3] S. Fassbinder, Practical Applications of Electrical Conductors, German Cooper Institute, 2010.
- [4] I.A. Ovid'ko, R.Z. Valiev, Y.T. Zhu, Review on superior strength and enhanced ductility of metallic nanomaterials, Prog. Mater. Sci. 94 (5) (2018) 462–540.
- [5] M.Y. Murashkin, I. Sabirov, X. Sauvage, R.Z. Valiev, Nanostructured Al and Cu alloys with superior strength and electrical conductivity, J. Mater. Sci. 51 (2016) 33–49.
- [6] J.R. Davis (Ed.), Aluminium and Aluminium Alloys Handbook, ASM International 1993, p. 784.
- [7] M.F. Ashby, Hybrids to fill holes in material property space, Philos. Mag. (2005), 85, 3235–3257; M.F. Ashby, In *Materials Selection in Mechanical Design*, 3d edition, Elsevier, Oxford 2005.
- [8] M.F. Ashby, Y.J.M. Bréchet, Designing hybrid materials, Acta Mater. 51 (19) (2003) 5801–5821.
- [9] O. Bouaziz, Y. Brechet, J.D. Embury, Heterogeneous and architected materials: a possible strategy for design of structural materials, Adv. Eng. Mater. 10 (2008) 21–36.
- [10] Z. Taiji, M. Yurong, C. Kai, et al., Structure and mechanical properties of a pteropod shell consisting of interlocked helical aragonite nanofibers, Angewandte Chemie-International Edition 50 (44) (2011) 10361–10365.
- [11] O. Bouaziz, S. Allain, D. Barcelo, R. Niang, Strengthening by plastic corrugated reinforcements: an effective way for strain-hardening improvement by architecture, Mater. Res. Soc. Symp. Proc. 1188 (2009).
- [12] J.H. Lienhard V, J.H. Lienhard IV, A Heat Transfer Textbook, Fourth edition Phlogiston Press, Cambridge, Massachusetts, USA, 2018 766 Publ.
- [13] H.-S. Kim, I.-S. Cho, J.-S. Shin, S.-M. Lee, B.-M. Moon, Solidification parameters dependent on interfacial heat transfer coefficient between aluminium casting and copper mold, ISIJ Int. 24 (2) (2005) 192–198.
- [14] Y. Ivanisenko, R. Kulagin, V. Fedorov, A. Mazilkin, T. Scherer, B. Baretzky, H. Hahn, High pressure torsion extrusion as a new severe plastic deformation process, Mater. Sci. Eng. A 664 (2016) 247–256.
- [15] Y. Qi, A. Kosinova, E. Lackin, V.V. Popov Jr., E. Rabkin, R. Lapovok, Effect of SPD processing on the strength and conductivity of AA6061 alloy, Adv. Eng. Mater. 1801370 (2019) 11.
- [16] Y. Beygelzimer, R. Kulagin, Y. Estrin, L.S. Toth, H.S. Kim, M.I. Latypov, Twist extrusion as a potent tool for obtaining advanced engineering materials: a review, Adv. Eng. Mater. 19 (8) (2017) <https://doi.org/10.1002/adem.201600873>.
- [17] J.L. Murray, The aluminium-copper system, International Metals Reviews 30 (1) (1985) 211–233.
- [18] N. Ponweiser, C.L. Lengauer, K.W. Richter, Re-investigation of phase equilibria in the system Al-Cu and structural analysis of the high-temperature phase η_1 -Al₁₁-Cu, Intermetallics 19 (2011) 1737–1746.
- [19] D.M. Rabkin, V.R. Ryabov, A.V. Lozovskaya, V.A. Dovzhenko, Preparation and properties of copper-aluminum intermetallic compounds, Powder Metallurgy and Metal Ceramics 9 (8) (1970) 695–700.
- [20] C. Maccioni, J.A. Rayne, S. Sen, C.L. Bauer, Low temperature resistivity of thin film and bulk samples of CuAl₂ and Cu₉Al₄, Thin Solid Films 81 (1981) 71–78.
- [21] S. Pfeifer, S. Großmann, R. Freudenberger, H. Willing, H. Kappl, Characterization of intermetallic compounds in Al-Cu-bimetallic interfaces, IEE 58th Holm Conference on Electrical Contacts (Holm), 2012 <https://doi.org/10.1109/HOLM.2012.6336554>.
- [22] F. d'Heurle, C. Alliot, J. Angilello, V. Brusic, J. Dempsey, D. Irmischer, The deposition by evaporation of Cu-Al alloy films, Vacuum 27 (4) (1977) 321–327.
- [23] M. Braunovic, L. Rodrigue, D. Gagnon, Nanoindentation study of intermetallic phases in Al-Cu bimetallic system, IEE 54th Holm Conference on Electrical Contacts (Holm), 2008 <https://doi.org/10.1109/HOLM.2008.ECP.55>.
- [24] <http://eddy-current.com/conductivity-of-metals-sorted-by-resistivity/> 2019.
- [25] R. Marstatt, M. Krutzlinger, J. Luderschmid, M.F. Zaeh, F. Haider, Formation of a diffusion-based intermetallic interface layer in friction stir welded dissimilar Al-Cu lap joints, IOP Conf. Ser. Mater. Sci. Eng. 181 (2017) (Paper Number: 012002).
- [26] S. Khoddam, Y. Estrin, H.S. Kim, O. Bouaziz, Torsional and compressive behaviour of a hybrid material: spiral fibre reinforced metal matrix composite, Mater. Des. 85 (2015) 401–411.
- [27] O. Bouaziz, Geometrically induced strain hardening, Scr. Mater. 68 (2013) 28–30.
- [28] R. Lauder, Electrical conductivity in inhomogeneous media, in: J.C. Garland, D.B. Tanner (Eds.), American Institute of Physics Conference Proceedings, 40, American Institute of Physics, NY 1978, pp. 2–45, Publisher.
- [29] D.S. McLachlan, M. Blaszkiewicz, R.E. Newnham, Electrical resistivity of composites, J. Am. Ceram. Society 73 (8) (1990) 2187–2203.